Numerical study of forced convection near a surface covered with hair

J. L. Lage and A. Bejan
Department of Mechanical Engineering and Materials Science, Duke University, Durham, NC, USA

This article reports the results of a numerical study of heat transfer to the air permeating through hair strands covering a flat surface. First, the surface is modeled as isothermal, and second the surface is assumed covered with uniform heat flux. For both models, the investigation develops dimensionless charts for calculating the overall heat transfer rate through a flat surface of finite size. The heat transfer rate is the sum of the direct heat transfer from the surface to air flow and the heat conducted away by the hair strands. In each model, the overall Nusselt number emerges as a function of four dimensionless groups. When the surface is sufficiently long, the constant flux-surface Nusselt number is up to 20% greater than the Nusselt number of the corresponding isothermal surface.

Keywords: porous media; hair; fibers on a surface

Introduction

The mechanism of heat transfer from a surface covered with hair is a combination of direct heat transfer between the surface and the adjacent air and the heat conducted away by the hair strands. The heat transfer behavior of each hair-strand is similar to that of a fin (cylindrical spine) on a plane heat exchanger surface.[1] The thermal conductivity of hair is more than ten times greater than that of air. The overall heat transfer process is therefore complicated not only by the lack of local thermal equilibrium between the hair strand and the immediate interstitial air, but also by the antagonistic heat transfer functions served by the air and the hair strand. The air flow is slowed, which tends to decrease the overall heat transfer rate, while the hair tends to augment it.

The purpose of the present study is to develop quantitative means for calculating the overall heat transfer rate through a plane surface covered with perpendicular strands of hair. Two surface models are considered: first, the surface is modeled as isothermal; second, the surface is assumed covered by a spatially uniform heat flux. In both models the heat transfer process is analyzed numerically.

Isothermal surface model

Consider the temperature distribution in the vicinity of a plane surface covered by perpendicular hair strands of uniform density n (strands/m^2), as shown in Figure 1. The surface temperature T_0 is constant. Away from the surface, the local temperature of the hair strand $T_s(x, y)$ differs from the temperature of the interstitial air $T_a(x, y)$. This heat transfer process is an example of forced convection through a porous medium saturated with fluid.[2–7] Unlike in the homogeneous model, which is employed in most studies of convection through porous media, in the present model the fluid (air) and the solid matrix (hair) are not in local thermal equilibrium.

We assume that the interstitial air flows parallel to the isothermal surface with uniform velocity U. This velocity is averaged only over the space occupied by air. The initial (starting) temperature of the air stream is uniform and equal to the ambient temperature T_∞. In the air thermal boundary-layer region, the conservation of energy requires

$$\rho c_p U \frac{\partial T_a}{\partial x} = k_a \frac{\partial^2 T_a}{\partial y^2} + nhp_s(T_s - T_a) \tag{1}$$

where p_s and h are the perimeter of the strand cross section and the strand-air heat transfer coefficient, respectively. The second term on the right-hand side of Equation 1 accounts for the air volumetric heating effect associated with the presence of warmer hair strands throughout the air stream. The air is treated as a Newtonian fluid with constant properties.

The heat transfer through each hair can be modeled as one-dimensional (1-D) conduction in the y direction. For a strand located at the downstream position x, the strand temperature distribution $T_s(x, y)$ is governed by the energy equation:

$$k_s A_s \frac{\partial^2 T_s}{\partial y^2} - hp_s(T_s - T_a) = 0 \tag{2}$$

where A_s is the area of the strand cross section. The second term in Equation 2 is the local cooling effect on the hair strand, as a reflection of the air heating effect accounted for in Equation 1.

It is convenient to make Equations 1 and 2 nondimensional:

$$\frac{\partial \theta_a}{\partial \xi} = \frac{1}{B}\frac{\partial^2 \theta_a}{\partial \eta^2} + \theta_s - \theta_a \tag{3}$$

$$\frac{\partial^2 \theta_s}{\partial \eta^2} = \theta_s - \theta_a \tag{4}$$

by defining the dimensionless variables

$$\xi = \frac{x}{\rho c_p U/nhp_s} \qquad \eta = \frac{y}{(k_s A_s/hp_s)^{1/2}} \tag{5}$$

$$\theta_s = \frac{T_s - T_\infty}{T_0 - T_\infty} \qquad \theta_a = \frac{T_a - T_\infty}{T_0 - T_\infty} \tag{6}$$

Group B of Equation 3 is related to the ratio of thermal conductivities k_s/k_a, or

$$B = nA_s \frac{k_s}{k_a} \tag{7}$$

Address reprint requests to Professor Bejan at the Department of Mechanical Engineering and Materials Science, Duke University, Durham, NC 27706, USA.

Received 5 December 1989; accepted 25 March 1990

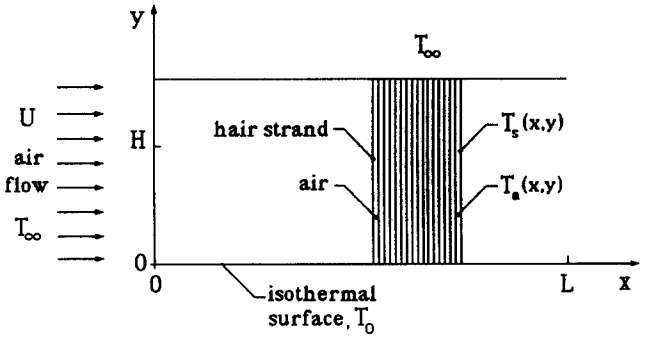

Figure 1 Two-dimensional model of an isothermal surface covered with perpendicular hair strands of uniform density

The boundary conditions that must be satisfied by the dimensionless temperatures $\theta_a(\xi, \eta)$ and $\theta_s(\xi, \eta)$ are

$$\theta_a = 0 \quad \text{at} \quad \xi = 0 \tag{8}$$

$$\theta_a = \theta_s = 1 \quad \text{at} \quad \eta = 0 \tag{9}$$

$$\theta_a, \theta_s \to 0 \quad \text{as} \quad \eta \to \infty \tag{10}$$

The starting condition for θ_s at $\xi = 0$ is obtained by solving Equation 4, subject to conditions 8–10. The result is

$$\theta_s(0, \eta) = \exp(-\eta) \tag{11}$$

which is the correct (and well-known) solution for the steady-state temperature distribution in a long fin with constant h and T_∞. Such a fin is the one situated in the $x = 0$ plane in Figure 1. One reviewer of this manuscript suggested using $\theta_s(0, \eta) = 0$ instead of Equation 11. However, θ_a is also zero at $\xi = 0$, so this alternative would lead to calculating nothing but the values $\theta_s = \theta_a = 0$ throughout the (ξ, η) domain, as we approach larger ξ values. Furthermore, the $\theta_s(0, \eta) = 0$ alternative is incompatible with Equation 6, which states that the leading-edge skin temperature is T_0.

Numerical method

We solved numerically the problem stated in Equations 3–11, using finite-difference approximations of the governing equations. We covered the numerical domain with a uniform grid in the longitudinal direction ξ and with a nonuniform grid in the transversal direction η. The nonuniformity of the latter is described by

$$\eta_j + 1 = \eta_j + \alpha_s^j \Delta \tag{12}$$

in which η_j is the η location of the jth grid line, Δ is the first (smallest) step size, and α_s is the rate of grid stretching. This grid provided a higher concentration of nodes in the vicinity of the $\eta = 0$ wall than far from the wall, in order to capture the boundary-layer characteristics of the θ_a and θ_s temperature distributions.

The discrete forms of Equations 3 and 4 are

$$\varepsilon\theta_{s_{i+1,j-1}} - [1 + \varepsilon + \tfrac{1}{2}(\Delta\eta_{j+1}^2 + \Delta\eta_{j+1}\,\Delta\eta_j)]\theta_{s_{i+1,j}} + \theta_{s_{i+1,j+1}} = -\tfrac{1}{2}(\Delta\eta_{j+1}^2 + \Delta\eta_{j+1}\,\Delta\eta_j)\theta_{a_{i+1,j}} \tag{13}$$

$$\theta_{a_{i+1,j}} = \theta_{a_{i,j}} + \Delta\xi\left[\frac{2}{B}\left(\frac{\theta_{a_{i,j+1}} - (1+\varepsilon)\theta_{a_{i,j}} + \varepsilon\theta_{a_{i,j-1}}}{\Delta\eta_{j+1}^2 + \Delta\eta_{j+1}\,\Delta\eta_j}\right) + (\theta_{s_{i,j}} - \theta_{a_{i,j}})\right] \tag{14}$$

in which i and j refer to steps in the ξ and η directions, respectively. The coefficient ε accounts for the local nonuniformity of the grid in the η direction; that is,

$$\varepsilon = \frac{\Delta\eta_{j+1}}{\Delta\eta_j} \tag{15}$$

Notation

A_s	Area of hair strand cross section
B	Modified conductivity ratio, Equations 7 and 26
C	Coefficient, Equation 28
c_P	Air-specific heat at constant pressure
D	Diameter of hair strand
e_a, e_s	Truncation errors, Equations 20 and 21
h	Strand-air heat transfer coefficient
H	Transversal dimension of computational domain
i	Step in the ξ direction
j	Step in the η direction
k_a	Air thermal conductivity
k_s	Strand thermal conductivity
k_z	Constant of order 100, Equations 42 and 43
L	Length of surface swept by air flow
n	Number of hair strands per unit area
Nu	Overall Nusselt number, isothermal surface, Equation 22
$\widetilde{\text{Nu}}$	Overall Nusselt number, constant-flux surface, Equation 41
p_s	Perimeter of hair strand cross section
q_a'	Total heat transfer rate to the air in contact with the $y = 0$ surface, per unit length in the direction normal to the plane of Figure 1, Equation 24
q_s'	Total heat transfer rate to the hair strands, per unit length in the direction normal to the plane of Figure 1, Equation 23
q''	Constant heat flux, Equation 31
q_a''	Heat flux to the air in contact with the $y = 0$ surface, Equation 32
q_s''	Heat flux to the root of the hair strand, Equation 32
T_a	Local air temperature
T_s	Local hair strand temperature
T_0	Temperature of $y = 0$ surface
$T_{0,\text{avg}}$	L-averaged temperature of $y = 0$ surface
T_∞	Ambient air temperature
U	Air velocity
x	Longitudinal coordinate, Figure 1
y	Transversal coordinate, Figure 1

Greek symbols

α	Air thermal diffusivity
α_s	Rate of griding stretching
Δ	Size of the smallest step in the η direction
ε	Grid nonuniformity parameter, Equation 15
η	Dimensionless transversal coordinate, Equation 5
η_H	Dimensionless transversal extent of computational domain, Equation 17
θ_a	Dimensionless air temperature, Equation 6
$\widetilde{\theta}_a$	Dimensionless air temperature, Equation 35
θ_s	Dimensionless strand temperature, Equation 6
$\widetilde{\theta}_s$	Dimensionless strand temperature, Equation 35
ξ	Dimensionless longitudinal coordinate, Equation 5
ξ_L	Dimensionless longitudinal extent of computational domain, Equation 16
ρ	Air density
ϕ	Porosity, Equation 25

Equation 13 represents a system of $(m-2)$ linear equations in θ_s, where m is the total number of grid lines in the η direction. The coefficient matrix of this system has a tridiagonal form; we therefore solved the system using a tridiagonal matrix algorithm.

In the first step of the numerical algorithm, Equation 3 was solved for θ_a by advancing in the ξ direction. Equation 4 was solved next for θ_s as a function of η. This procedure was repeated until ξ reached the downstream extremity of the isothermal surface $x=L$, which corresponds to the dimensionless number

$$\xi_L=\frac{L}{\rho c_P U/nhp_s} \tag{16}$$

In the transversal direction, the computational domain was extended to $y=H$, or

$$\eta_H=\frac{H}{(k_sA_s/hp_s)^{1/2}} \tag{17}$$

Zero flux boundary conditions were imposed on the $\eta=\eta_H$ boundary, $\partial\theta_a/\partial\eta=\partial\theta_s/\partial\eta=0$. The η_H value was increased until the calculated θ_a and θ_s values on the $\eta=\eta_H$ boundary were less than 10^{-4}, in accordance with the proper boundary conditions of Equation 10. Representative values of η_H are listed in Table 1.

With reference to Equation 3, the von Neumann stability analysis[8] recommends the following stability criteria:

$$0.3\le\Delta\xi\left(1+\frac{2(1+\varepsilon)}{B\Delta^2}\right)\le 1.7 \tag{18}$$

$$\frac{\Delta\xi(\varepsilon-1)}{B\Delta^2}\le 0.7 \tag{19}$$

In the derivation of these criteria, the denominator on the right-hand side of Equation 14 was replaced (approximately) with Δ. This is a conservative approximation, because $\Delta\eta$ becomes progressively larger than Δ as j increases. Worth noting also is the fact that criterion 18 is more restrictive than criterion 19, because $1<\varepsilon<2$. Numerical tests confirmed that inequalities 18 and 19 provide reliable descriptions of the bounds of numerical stability.

The truncation errors associated with the discrete Equations 13 and 14 are

$$e_a=O[\Delta\xi(\Delta\eta_{j+1}-\Delta\eta_j)]+O(\Delta\xi^2) \tag{20}$$

$$e_s=O(\Delta\eta_{j+1}-\Delta\eta_j) \tag{21}$$

As the e_a and e_s errors are proportional to the local η derivatives of the solutions—and as the θ_a and θ_s profiles have their sharpest slopes at $\eta=0$—the accuracy of the solution was based on tests at the $\eta=0$ surface. The surface parameter used in these tests was the overall Nusselt number:

$$\mathrm{Nu}=\frac{q_s'+q_a'}{k_a(T_0-T_\infty)} \tag{22}$$

in which q_s' and q_a' represent the total heat transfer rates from the T_0 surface to all the hair-strand roots and to the air that comes in direct contact with the surface:

$$q_s'=\int_0^L A_sk_s\left(-\frac{\partial T_s}{\partial y}\right)_{y=0} n\,dx \tag{23}$$

$$q_a'=\int_0^L k_a\left(-\frac{\partial T_a}{\partial y}\right)_{y=0}\phi\,dx \tag{24}$$

The ϕ factor in Equation 24 is the porosity of the porous medium formed by the hair strands, or

$$\phi=1-nA_s \tag{25}$$

The modified conductivity ratio B of Equation 7 is therefore proportional to the solid fraction $(1-\phi)$:

$$B=(1-\phi)\frac{k_s}{k_a} \tag{26}$$

Combining Equations 22–24 leads to the following Nusselt number integral:

$$\mathrm{Nu}=-C\int_0^{\xi_L}\left(\frac{\partial\theta_s}{\partial\eta}+\frac{\phi}{B}\frac{\partial\theta_a}{\partial\eta}\right)_{\eta=0}d\xi \tag{27}$$

in which C is shorthand for the group:

$$C=\frac{U}{\alpha}\left(\frac{k_sA_s}{hp_s}\right)^{1/2} \tag{28}$$

We performed accuracy tests for every value of the parameter B, using relatively high values of ϕ and ξ_L. These tests are summarized in Table 1. The strand-temperature truncation error e_s tends to dominate the air-temperature truncation error e_a. In all the cases these errors are small enough that the overall Nusselt number does not change by more than 4%. In the end, the number of nodes we chose in the η direction was 29. The number of nodes selected for the ξ direction varied with both B and ξ_L.

The use of a nonuniform grid in the η direction is not a rigid requirement, especially when the cost effectiveness of the numerical code is not important. In the present study, the efficiency of the code was important, which led to our use of a finer mesh near the surface, where all the temperatures decayed almost exponentially. Taking the case of $B=0.1$ and $\phi=0.9$ as

Table 1 The effect of grid fineness on the accuracy of the numerical solution ($\phi=0.9$, $\xi_L=10$)

B	η_H	Nodes ξ	Nodes η	Δ	ε	CPU(s)	e_a	e_s	Nu
0.1	60	500	14	0.8	1.2625	27	4.6×10^{-3}	2.1×10^{-1}	10.44
		2,000	29	0.4	1.1064	124	2.4×10^{-4}	4.3×10^{-2}	10.58
		6,250	58	0.2	1.0498	431	1.8×10^{-5}	9.9×10^{-3}	10.66
1	30	200	14	0.4	1.2625	19	8.0×10^{-3}	1.1×10^{-1}	4.55
		800	29	0.2	1.1065	87	4.2×10^{-4}	2.1×10^{-2}	4.64
		2,500	58	0.1	1.0498	176	3.6×10^{-5}	5.0×10^{-3}	4.69
10	25	25	14	0.4	1.2365	—	2.0×10^{-1}	9.5×10^{-2}	3.20
		100	29	0.2	1.0960	12	1.2×10^{-2}	1.9×10^{-2}	3.45
		500	58	0.1	1.0450	51	4.9×10^{-4}	4.5×10^{-3}	3.55
100	20	20	14	0.2	1.304	—	8.8×10^{-1}	6.1×10^{-2}	3.07
		50	29	0.1	1.1227	7	4.2×10^{-2}	1.2×10^{-2}	3.30
		200	58	0.05	1.0573	28	2.6×10^{-3}	2.9×10^{-3}	3.42

an example, if the near-surface grid is extended all the way to the outer limit, η_H, we would have had to use 300 nodes in the η direction instead of only 58 (see Table 1).

Heat transfer from an isothermal surface

Figures 2 and 3 show the chief characteristics of the air- and strand-temperature distributions. The strand temperature θ_s is at every ξ and η greater than the air temperature θ_a; however, the difference $(\theta_s-\theta_a)$ decreases as both ξ and η increase. The shapes of the θ_s and θ_a profiles can be approximated well by exponential-decay functions in η. The $\partial\theta_s/\partial\eta$ and $\partial\theta_a/\partial\eta$ gradients at the $\eta=0$ surface decrease in the downstream direction ξ.

The four frames in Figures 2 and 3 were arranged to illustrate the effects of the additional parameter of the solution, B. Worth keeping in mind is that the porosity parameter ϕ (as distinct from the parameter B) has no effect on the θ_s and θ_a distributions, as can be seen by examining the problem statement, Equations 3–11. The porosity ϕ influences the temperature solutions only through the parameter B, as we showed in Equation 26.

Proceeding from Figure 2 to Figure 3, note that, as B increases, the η distance of thermal penetration along the hair strand decreases. However, the local discrepancy between θ_s and θ_a increases as B increases. In fact, in the low-B case of Figure 2, the θ_s and θ_a values are nearly the same if ξ is greater than 2. In the high-B case of Figure 3, the discrepancy between θ_s and θ_a is noticeable even at $\xi=10$.

The overall Nusselt number Nu is a function of four parameters: B, ϕ, C, and ξ_L. The effect of each of these parameters is illustrated in Figure 4, in which the Nu/C ratio was plotted as a function of ξ_L and B for fixed porosities ϕ. To begin with, the Nusselt number is proportional to C; it then

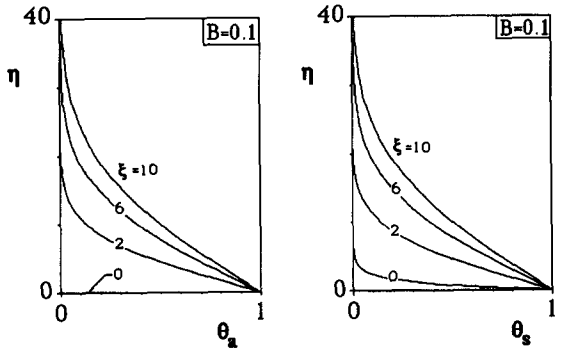

Figure 2 Temperature distribution in the air and hair strands near an isothermal surface ($B=0.1$)

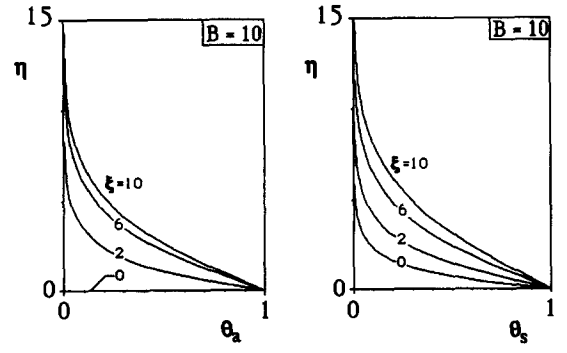

Figure 3 Temperature distribution in the air and hair strands near an isothermal surface ($B=10$)

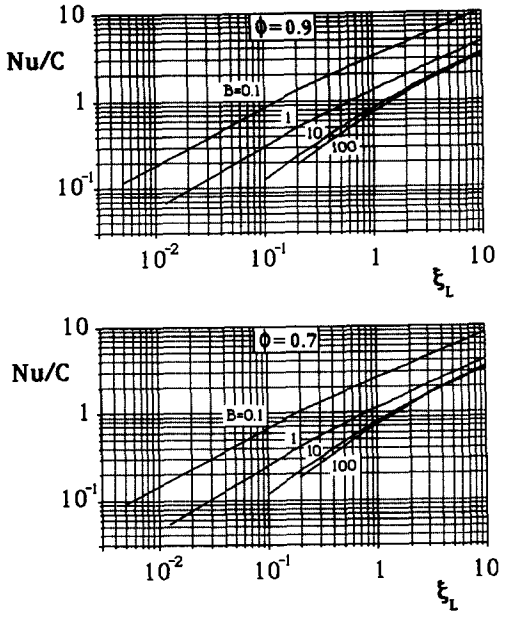

Figure 4 Overall Nusselt number for heat transfer from an isothermal surface covered with hair

increases monotonically with the dimensionless length of the isothermal surface ξ_L. The latter is approximated well by the power-law $\mathrm{Nu}\sim\xi_L^b$ where the b exponent takes values in the range 0.6–0.8.

The effect of increasing the modified conductivity ratio B is to decrease the overall Nusselt number. This effect is particularly strong in the B range 0.1–10. Above this range, the Nusselt number is practically insensitive to changes in the B parameter.

The porosity ϕ has only a minor impact on the Nusselt number. By comparing the two graphs of Figure 4, we note that Nu decreases by roughly 10 percent as ϕ decreases from 0.9 to 0.7.

The present Nu calculations permit us to evaluate the accuracy of the approximate analytical solution developed for the same problem in the earlier work.[1] The analytical solution was based on the assumption that the air thermal boundary-layer is much thinner than the distance of conduction penetration along the hair strand. It predicted a Nusselt number Nu that depends on only three parameters, C, ξ_L, and the ratio $\phi/B^{1/2}$; that is,

$$\mathrm{Nu}\cong C\left((2\xi_L)^{1/2}+1.22\frac{\phi}{B^{1/2}}\right] \tag{29}$$

The same analysis indicated that Equation 29 holds when B is large enough that

$$B\gtrsim 3\xi_L \tag{30}$$

In Figure 5 we compare the present Nu calculations and the prediction based on the analytical solution, Equation 29. The entire figure was constructed for the special case of $\phi/B^{1/2}=0.1$, in which Equation 29 reduces to a single curve of Nu/C versus ξ_L. The two lower curves were obtained numerically for two combinations of ϕ and B that satisfy the constraint $\phi/B^{1/2}=0.1$.

When comparing each of the numerical Nu curves with the theoretical curve based on Equation 29, keep in mind that the latter is valid only in the range dictated by the inequality 30. Thus when $B=25$ and $\phi=0.5$, the upper curve "ends" at a ξ_L value of order 10; in the other case, when $B=90.25$ and $\phi=0.95$, the right extremity of the upper curve is in the vicinity of $\xi_L\sim 30$. These limits are indicated by the vertical bars labeled (a) and (b) in Figure 5.

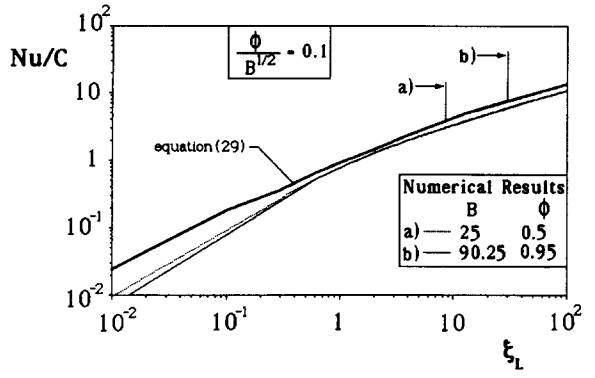

Figure 5 Comparison between the present numerical results and the approximate solution, Equation 29, for heat transfer from an isothermal surface

Agreement between the present calculations and the approximate solution, Equation 29, is quite good. It shows that the theoretical solution, Equation 29 can be used as a first-cut estimate of the total heat transfer rate through the isothermal surface and that it consistently overestimates the heat transfer rate. Agreement between theory and numerical results improves as B increases and as the ξ_L domain of the theoretical solution expands, cf. Equation 30.

Constant-flux surface model

The plane surface of Figure 1 can alternatively be modeled as a surface with uniform heat flux,

$$q'' = (1-\phi)q_s'' + \phi q_a'' = \text{Constant} \tag{31}$$

in which q_s'' and q_a'' are the heat fluxes to the hair root and to the air that touches the surface, respectively:

$$q_s'' = -k_s\left(\frac{\partial T_s}{\partial y}\right)_{y=0} \quad \text{and} \quad q_a'' = -k_a\left(\frac{\partial T_a}{\partial y}\right)_{y=0} \tag{32}$$

We can now describe the heat transfer through the two-temperature porous medium by the energy equations:

$$\frac{\partial \tilde{\theta}_a}{\partial \xi} = \frac{1}{B}\frac{\partial^2 \tilde{\theta}_a}{\partial \eta^2} + \tilde{\theta}_s - \tilde{\theta}_a \tag{33}$$

$$\frac{\partial^2 \tilde{\theta}_s}{\partial \eta^2} = \tilde{\theta}_s - \tilde{\theta}_a \tag{34}$$

in which $\tilde{\theta}_s$ and $\tilde{\theta}_a$ are the new dimensionless temperatures:

$$\tilde{\theta}_s = \frac{T_s - T_\infty}{(q''/k_a)(k_s A_s/hp_s)^{1/2}} \quad \text{and} \quad \tilde{\theta}_a = \frac{T_a - T_\infty}{(q''/k_a)(k_s A_s/hp_s)^{1/2}} \tag{35}$$

The boundary conditions that in this new formulation replace Equations 8–11 are

$$\tilde{\theta}_a = 0, \quad \text{at} \quad \xi = 0 \tag{36}$$

$$\tilde{\theta}_a = \tilde{\theta}_s, \quad \text{at} \quad \eta = 0 \tag{37}$$

$$-B\left(\frac{\partial \tilde{\theta}_s}{\partial \eta}\right)_{\eta=0} - \phi\left(\frac{\partial \tilde{\theta}_a}{\partial \eta}\right)_{\eta=0} = 1, \quad \text{at} \quad \eta = 0 \tag{38}$$

$$\tilde{\theta}_a, \tilde{\theta}_s \to 0 \quad \text{as} \quad \eta \to \infty \tag{39}$$

Particularly worth noting are the constant heat-flux condition, Equation 38 and that the surface temperature (unknown) is equal to both $\tilde{\theta}_a$ and $\tilde{\theta}_s$ at $\eta = 0$, Equation 37. Solving Equation 34 subject to Equations 36, 38, and 39 leads to a closed-form expression for the starting-temperature distribution along the hair strand (see also the alternative discussed under Equation 11):

$$\theta_s(0, \eta) = \frac{1}{B}\exp(-\eta) \tag{40}$$

Solutions for the temperature fields $\tilde{\theta}_s(\xi, \eta)$ and $\tilde{\theta}_a(\xi, \eta)$ were determined using the numerical method previously described. These solutions are influenced by two parameters: B and ϕ. Comparing the upper graphs with the corresponding lower graphs in Figure 6, we see that, as ϕ decreases from 0.9 to 0.7, the strand and air temperatures increase throughout the (ξ, η) domain. The temperature profiles again resemble exponentials, and the surface temperature increases monotonically in the downstream direction.

Figure 7 shows the effect of increasing the B parameter by three orders of magnitude. The η thickness of the boundary-layer region inhabited by air and hair strands decreases significantly. The local differences between $\tilde{\theta}_s$ and $\tilde{\theta}_a$ become more obvious as B increases: Note the much sharper $\partial\tilde{\theta}_a/\partial\eta$ gradient at $\eta = 0$ in Figure 7, compared to the corresponding $\partial\tilde{\theta}_s/\partial\eta$ gradient. At the other extreme, when B is small (Figure 6), the differences between $\tilde{\theta}_s$ and $\tilde{\theta}_a$ are almost imperceptible.

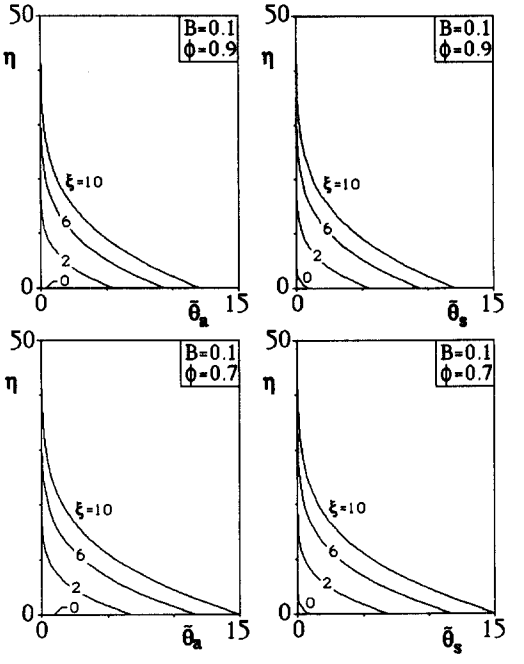

Figure 6 Temperature distribution in the air and hair strands near a constant-flux surface ($B = 0.1$)

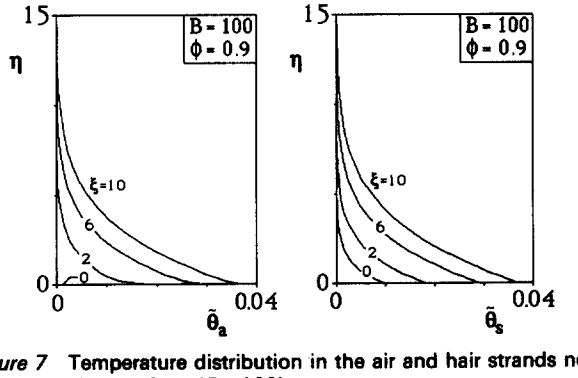

Figure 7 Temperature distribution in the air and hair strands near a constant-flux surface ($B = 100$)

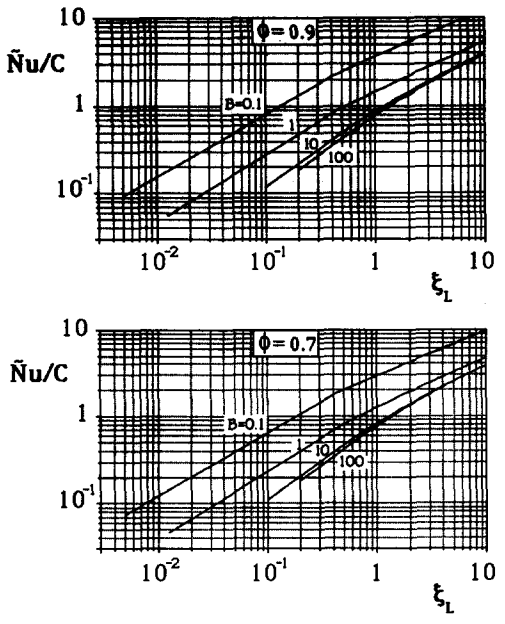

Figure 8 Overall Nusselt number for heat transfer from a constant-flux surface covered with hair

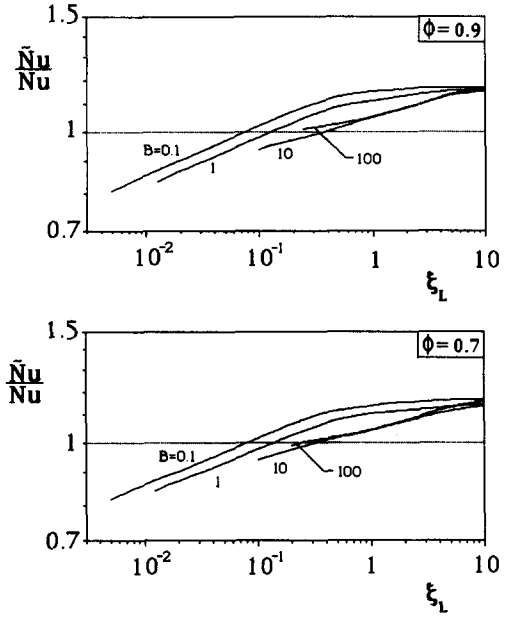

Figure 9 Discrepancy between the overall Nusselt numbers for the isothermal-surface and constant-flux-surface models

Comparing the abscissa ranges of Figures 6 and 7, we note further that the dimensionless temperatures θ_s and θ_a decrease by almost three orders of magnitude as B increases from 0.1 to 100. This effect is described better by the Nusselt number based on the L-averaged surface–ambient temperature difference:

$$\tilde{Nu}=\frac{q''L}{k_a(T_{0,avg}-T_\infty)}=\frac{C}{B}\xi_L\left[\frac{1}{\xi_L}\int_0^{\xi_L}\tilde{\theta}_a(\xi,0)\,d\xi\right]^{-1} \tag{41}$$

in which the quantity in the brackets is the dimensionless temperature of the $\eta=0$ surface, averaged over the distance ξ_L. According to this definition, the overall Nusselt number Nu emerges as a function of four parameters: C, ξ_L, B, and ϕ.

The overall Nusselt number for the constant-flux surface is presented in chart form in Figure 8. We intentionally constructed the two graphs of Figure 8 in the style of Figure 4, in order to show the similar qualitative behaviors of Nu and Nu. The constant-flux Nusselt number increases appreciably in the downstream direction and decreases as B increases. The porosity of the hair-strand matrix has only a minor effect on Nu.

The similarity between the isothermal-surface and constant flux-surface Nusselt numbers is stressed further by Figure 9. It shows that Nu and Nu differ only within $\pm 20\%$ in the parametric domain covered by the present numerical solutions: $0.1 \le B \le 100$, $0.01 < \xi_L < 10$, and $0.7 \le \phi \le 0.9$. At downstream positions ξ_L greater than approximately 0.1, the constant-flux Nusselt number is generally greater than the corresponding Nusselt number for the isothermal surface model.

Conclusions

In this study we focused on the fundamental mechanism of heat transfer through a surface covered with hair and developed numerical solutions for calculating the overall steady-state heat transfer rate through such a surface. The main results that summarize the contributions of this study are the following.

(1) The overall Nusselt number for an isothermal surface (Nu) depends on four parameters and can be evaluated using the charts of Figure 4.

(2) The theoretical solution, Equation 29, overestimates by up to 100% the numerical Nu results for the isothermal surface model.

(3) The overall Nusselt number for heat transfer from a constant-flux surface (Nu) depends on the same four parameters as Nu. The value of Nu can be estimated from the charts of Figure 8.

(4) In the limit of sufficiently long surfaces ($\xi_L \ge 0.1$), the constant-flux Nusselt number is within 20% greater than the isothermal-surface Nusselt number.

A final observation concerns the constants A_s, p_s, and h, whose values we assumed were known in the preceding discussion. These constants depend on the size of the hair strand. If each hair strand can be modeled as a long cylinder of diameter D, then $A_s=(\pi/4)D^2$ and $p_s=\pi D$. In addition, the earlier work[1] showed that if the air flow is slow enough to obey Darcy's law, the heat transfer coefficient is constant and approximately equal to:

$$h \cong \frac{k_z}{4}\frac{1-\phi}{\phi}\frac{k_a}{D} \tag{42}$$

in which the coefficient k_z on the right-hand side is approximately equal to 100. Numerical[9,10] and experimental[11] data for pressure drop across a bank of cylinders in cross flow have shown that, in the low Reynolds number limit, the permeability of the medium is correlated by a relationship of the Kozeny type:[12]

$$K \cong \frac{\phi^3 D^2}{k_z(1-\phi)^2} \tag{43}$$

We used this permeability function in the derivation of Equation 42.[1]

One reviewer of the original manuscript questioned our use of the constant-flux expression 31. This expression can be derived in the following way. Consider a small enough sample area of the skin surface and let A be its area. This area is made up of bare skin ($A_a=\phi A$) and an area occupied by the roots of the hair strands. There are nA strands; therefore their total root area is $nAA_s=(1-\phi)A$. The heat transfer rate through the

A-sized sample is

$$q''A = q''_a A_a + q''_s n A A_s \tag{44}$$

which, divided by A, becomes the same as Equation 31.

References

1 Bejan, A. Theory of heat transfer from a surface covered with hair. *J. Heat Transfer*, 1990, **112** (accepted for publication)

2 Vafai, K. and Tien, C. L. Boundary and inertia effects on flow and heat transfer in porous media. *Int. J. Heat Mass Transfer*, 1981, **24**, 195–203

3 Vafai, K. Convective flow and heat transfer in variable porosity media. *J. Fluid Mech.*, 1984, **147**, 233–259

4 Vafai, K. and Thiyagaraja, R. Analysis of flow and heat transfer at the interface region of a porous medium. *Int. J. Heat Mass Transfer*, 1987, **30**, 1391–1405

5 Poulikakos, D. and Kazmierczak, M. Forced convection in a duct partially filled with a porous material. *J. Heat Transfer*, 1987, **109**, 653–662

6 Poulikakos, D. and Renken, K. Forced convection in a channel filled with a porous medium including the effects of flow inertia, variable porosity and Brinkman friction. *J. Heat Transfer*, 1987, **109**, 880–888

7 Renken, K. J. and Poulikakos, D. Experiment and analysis of forced convective heat transport in a packed bed of spheres. *Int. J. Heat Mass Transfer*, 1988, **31**, 1399–1408

8 O'Brien, G. G., Hyman, M. A., and Kaplan, S. A study of the numerical solution of partial differential equations. *J. Math. Physics.*, 1950, **29**, 223–251

9 Happel, J. Viscous flow relative to arrays of cylinders. *AIChE J.*, 1959, **5**, 174–177

10 Eidsath, A., Carbonell, R. G., Whitaker, S., and Herrmann, L. R. Dispersion in pulsed systems III—Comparison between theory and experiments for packed beds. *Chem. Eng. Sci.*, 1983, **38**, 1803–1816

11 Mueller, A. C. Process heat exchangers. *Handbook of Heat Transfer Applications*, 2nd ed. (W. M. Rohsenow, J. P. Hartnett, and E. N. Ganic, Eds.), McGraw-Hill, New York, 1985

12 Cheng, P. Geothermal heat transfer. *Handbook of Heat Transfer Applications*, 2nd ed. (W. M. Rohsenow, J. P. Hartnett, and E. N. Ganic, Eds.), McGraw-Hill, New York, 1985